Journal of Biomedical Optics 5(1), 31–39 (January 2000)

Novel dental dynamic depth profilometric imaging using simultaneous frequency-domain infrared photothermal radiometry and laser luminescence

Lena Nicolaides
Andreas Mandelis
Photothermal and Optoelectronic Diagnostics Laboratories
Department of Mechanical and Industrial Engineering
University of Toronto
and
Materials and Manufacturing Ontario (MMO)
5 King's College Road
Toronto, Ontario M5S 3G8 Canada

Stephen H. Abrams
Four Cell Consulting
748 Briar Hill Avenue
Toronto, Ontario M6B 1L3, Canada

Abstract. A high-spatial-resolution dynamic experimental imaging setup, which can provide simultaneous measurements of laser-induced frequency-domain infrared photothermal radiometric and luminescence signals from defects in teeth, has been developed for the first time. The major findings of this work are (i) radiometric images are complementary to (anticorrelated with) luminescence images, as a result of the nature of the two physical signal generation processes; (ii) the radiometric amplitude exhibits much superior dynamic (signal resolution) range to luminescence in distinguishing between intact and cracked sub-surface structures in the enamel; (iii) the radiometric signal (amplitude and phase) produces dental images with much better defect localization, delineation, and resolution; (iv) radiometric images (amplitude and phase) at a fixed modulation frequency are depth profilometric, whereas luminescence images are not; and (v) luminescence frequency responses from enamel and hydroxyapatite exhibit two relaxation lifetimes, the longer of which (~ms) is common to all and is not sensitive to the defect state and overall quality of the enamel. Simultaneous radiometric and luminescence frequency scans for the purpose of depth profiling were performed and a quantitative theoretical two-lifetime rate model of dental luminescence was advanced.
[S1083-3668(00)00601-8]

Keywords: dental infrared photothermal radiometry; photothermal imaging; luminescence.

Paper JBO-90012 received Mar. 8, 1999; revised manuscript received July 20, 1999; accepted for publication Sep. 27, 1999.

1 Introduction

In recent years, rapidly increasing research activities have been reported centered on laser-induced luminescence as a probing technique for the detection and quantification of physical and chemical processes associated with carious dental enamel. In general, luminescence suffers from low signal levels and thus in most cases dyes are used to enhance sensitivity.[1] Under laboratory conditions, the results appear satisfactory, yet the use of dyes makes the method difficult for clinical applications. Another promising approach is laser-scanned fluorescence (or luminescence). This technique can detect early carious lesions[2] by producing surface images which are subsequently enhanced via standard image processing techniques.[3] Nevertheless, the relatively low signal-to-noise ratio (SNR) limits the contrast and the diagnostic ability of laser fluorescence. In this work, frequency-domain infrared photothermal radiometry (FD-PTR) and modulated laser luminescence are introduced as complementary dynamic dental diagnostic tools for quantifying sound and defective (cracked) enamel. This work is intended to show the complementarity between modulated luminescence and photothermal frequency scans and imaging. As a first test for investigating the sensitivity and spatial resolution of the methodology as applied to dental tissues, cracked and sound enamel samples were chosen. The significance to dentistry lies on the conclusions regarding the potential of this technique to monitor dental lesions at the early stages of carious decay where lateral and subsurface spatial resolution on the order of the crack sizes and subsurface depths investigated in this work (100–300 μm) may be required.

FD-PTR is a growing technology for the nondestructive evaluation (NDE) of subsurface features in opaque materials.[4,5] It has also shown promise in the study of excited-state dynamics in active optically transparent solid-state (laser) materials.[6] The technique is based on the modulated thermal infrared (blackbody or Planck-radiation) response of a medium, resulting from radiation absorption, nonradiative energy conversion, and excited-to-ground-state relaxation, followed by temperature rise. The generated signals carry subsurface information in the form of a temperature depth integral. As a result, PTR has the ability to penetrate and yield information about an opaque medium well below the range of optical imaging. Owing to this ability, pulsed-laser PTR has been extensively used with turbid media such as tissue[7,8] to study the subsurface deposition localization of laser radiation,

Address correspondence to Andreas Mandelis; electronic mail: mandelis@mie.utoronto.ca

1083-3668/2000/$15.00 © 2000 SPIE

a task which is difficult or impossible for optical methods due to excessive scattering. Very recently, dental applications of pulsed PTR focused on the diagnostics of dentin and enamel have been reported.[9,10] These preliminary studies have examined the temperature behavior of dental tissues, their tolerance to optical-to-thermal energy conversion and deposition, and their ablation threshold by high-fluence pulsed lasers. Unfortunately, the high-fluence deposition and wideband nature of pulsed photothermal detection, coupled with laser-pulse jitter and the high noise content inherent to all thermal (incoherent) signal techniques, prohibits the nondestructive application of this PTR mode to dental imaging, at least in competition with luminescence and other imaging diagnostics. FD-PTR, on the other hand, exhibits much higher SNR than its pulsed counterpart[11] and a fixed probe depth with the use of a single modulation frequency. A convenient source of energy is the laser beam, which can be easily modulated and focused to yield a coherent localized energy source. The basic ingredients of an FD-PTR dental microscope are a source of energy, a physical scatterer (the tooth), and a detector of the radiation scattered by the tooth. For an image to be formed, either the source or the detector must be localized. Photothermal imaging generally falls into the category of scanned microscopy with a localized source. The current experimental method is based on low-fluence photothermal radiometric detection microscopy,[12] which detects the emission of infrared radiation from a heated region of the sample without thermally altering it. A temperature oscillation due to modulated heating causes a variation in the thermal emissions, which is monitored using an infrared detector. The temperature modulation allows for thermal energy to reach the surface diffusively from a depth approximately equal to a thermal wavelength, $\lambda_{th}(f) = 2\pi\sqrt{\alpha/\pi f}$, where α is the material thermal diffusivity (cm^2/s) and f is the laser-beam modulation frequency. Scatterers located within a fraction of a thermal wavelength from the source dominate the contrast of radiometric images. In this way, when the thermal wavelength is varied, e.g., by changing the laser-beam modulation frequency, the region of the specimen that contributes to the image is also varied.

In this work, infrared radiometric and luminescence images of flat enamel surfaces from teeth with subsurface lesions (cracks) were obtained at a fixed laser-intensity modulation frequency. Furthermore, a hydroxyapatite reference sample was used for quantitative comparison with enamel-generated signals.

2 Materials and Methods

2.1 Sample Preparation

Extracted molar teeth being stored in water were selected as samples. The samples bore no visible caries on their buccal or lingual surfaces. The teeth were disinfected with Hibitane (2% chlorhexidine), washed with water and any surface pellicle or stain was removed using a rubber cup prophylaxis with coarse grit prophy paste. The roots were removed and each tooth was sectioned in half. At that point, the dentin was removed from the inner half of the section until very little remained, leaving specimens of between one and two millimeters in thickness. The samples were then stored in a humid environment with distilled water to avoid dehydration and contamination. Before irradiation, the teeth were dried and the surfaces examined to identify the regions of cracks and fissures. These regions were chosen as good candidates for near-surface and subsurface crack investigation. An extracted molar without any dentin removal and a hydroxyapatite sample was investigated as reference. The hydroxyapatite was chosen since this compound consists of approximately 90% in tooth enamel.

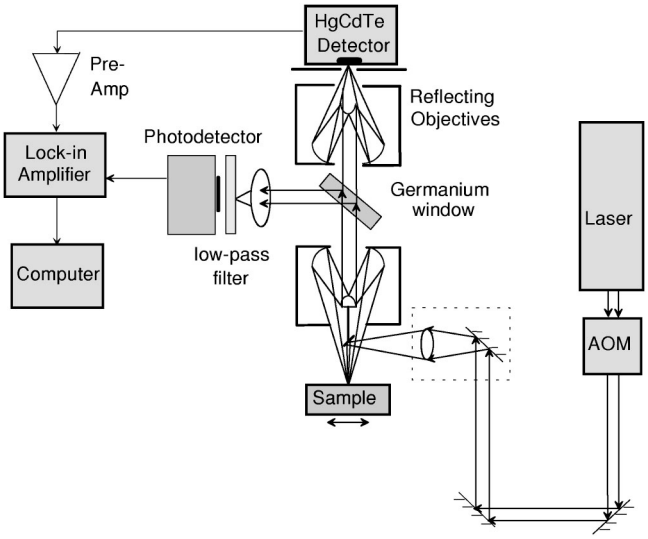

Fig. 1 Frequency-domain photothermal radiometric (FD-PTR) and luminescence imaging instrumentation. HgCdTe: mercury-cadmium-telluride infrared detector; AOM: acousto-optic modulator.

2.2 Experimental System

The experimental setup for performing simultaneous FD-PTR and luminescence studies is shown in Figure 1. A 488 nm wavelength cw Innova 100 Ar^+ laser from coherent is modulated by an external acousto-optic modulator (AOM-Isomet 1201E-1) at frequency $f = \omega/2\pi$, where ω is the angular modulation frequency. The laser beam is then focused with a high performance lens (Gradium GPX085) onto a sample to a spot size of approximately 30 μm in reflection, at an incident power of 0.1 W. The blackbody radiation from the optically excited sample is collected, collimated, and focused to a fine spot size by two axially aligned reflecting objectives (Ealing 25-0522X36 and 25-0506X15) onto a liquid-nitrogen-cooled HgCdTe (mercury-cadmium-telluride) detector (EG&G Judson J15D12-M204-S050U). The HgCdTe detector is a photoconductive element, which undergoes a change in resistance proportional to the intensity of the incident infrared radiation. It has an active square size area of 50 μm$\times$50 μm and a spectral bandwidth of 2–12 μm. Its efficiency increases with decreasing temperature, so the detector is operated at a cryogenic temperature of 77 K. An antireflection (AR)-coated germanium window with a transmission bandwidth of 2–14 μm is mounted in front of the detector to block any visible radiation from the pump laser. Before being sent to the digital lock-in amplifier (Stanford Research System Model SR850), the photothermal radiometric signal is amplified by a preamplifier with a frequency bandwidth dc 1 MHz (EG&G Judson Model PA-300), especially designed for operation with the HgCdTe detector. Since both the modulated heating source

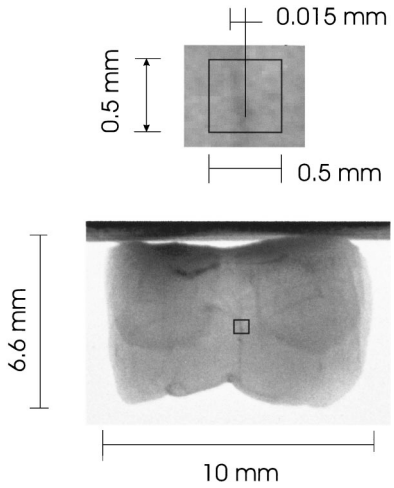

Fig. 2 Backilluminated photograph of a flat enamel slice with a 15 μm wide transverse crack.

and the detector are localized, they can be scanned across the sample. To perform PTR imaging, the sample is moved in a raster fashion. This process of data acquisition, storage, and scanning is automated. For the simultaneous measurement of luminescence and PTR signal, a germanium window was placed between the path of the two reflective objectives. The germanium window was utilized so that wavelengths up to 900 nm would be reflected and the infrared radiation would be transmitted to the second reflecting objective focused onto the infrared detector. The reflected spectrum was focused onto a photodetector of spectral bandwidth 300 nm–1.1 μm (Newport 818-BB-20). A cut-off colored glass filter (Schott OG570) was placed in front of the photodetector to supress scattered laser light and the spectrally integrated enamel luminescence following excitation by the 488 nm laser light[13] was monitored. In order to test if any experimental components showed fluorescence, a measurement with a mirror as a sample was performed. The result was negative (no signal).

Following optical absorption of laser photons, the experimental setup can monitor simultaneously and independently the nonradiative (optical-to-thermal) conversion *via* infrared photothermal radiometry, and the radiative deexcitation *via* luminescence emission. With this experimental setup, two types of experiments can be performed. The first is imaging, where the sample coordinates are scanned at a constant frequency. The second experiment is dynamic, performed at one location on the sample. It generates depth-dependent information by scanning the laser-beam modulation frequency (''a frequency scan'').

3 Results and Discussion

3.1 PTR and Luminescence Imaging

Simultaneous PTR and luminescence images were obtained at different modulation frequencies and in all reported images, the signal ranges between high (black) and low (light gray). A flat enamel slice with a single 15 μm wide transverse crack was backilluminated with a 25 W fluorescent light on a white plexiglas screen background and photographed with a 135 mm macro-lens, shown in Figure 2. The enamel slice is 2 mm thick and 6 mm$\times$10 mm in size. The first image set at f = 20 Hz is aimed to show the intrinsic features of and anticorrelation between PTR and luminescence images. The results are shown in Figure 3. Figure 3(a) is a 0.5 mm$\times$0.5 mm luminescence image of the flat enamel slice with a near vertical subsurface crack as marked in Figure 2. The luminescence image seems to be sensitive to the presence of the crack; in the cracked region, the luminescence

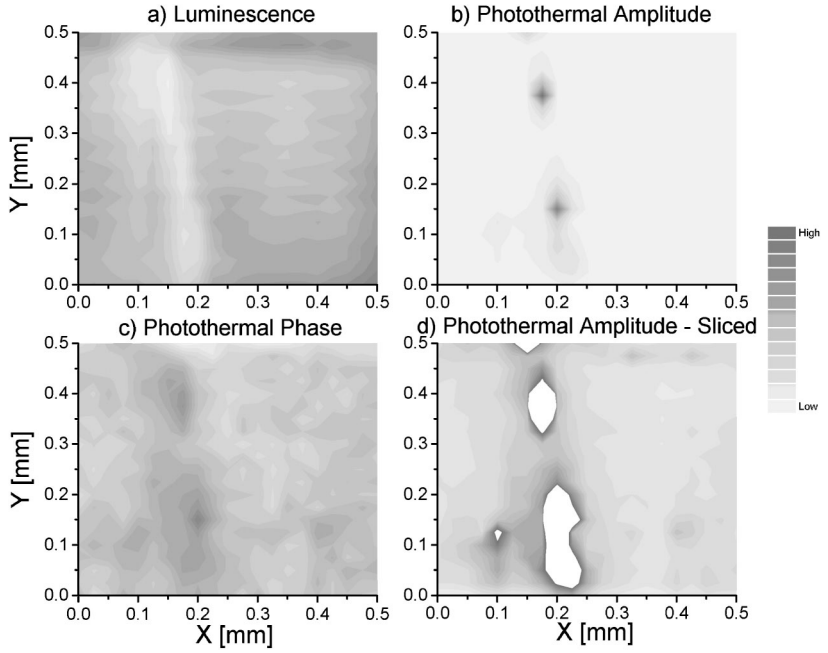

Fig. 3 Simultaneous luminescence and FD-PTR images at f=20 Hz. (a) Luminescence amplitude, (b) PTR amplitude, (c) PTR phase, and (d) PTR amplitude with peaks sliced off.

signal is low (light gray), whereas in the (nearly) intact region, the luminescence is relatively high (gray). Within the crack region, luminescence photon emission of several wavelengths characteristic of the enamel chromophores is essentially absent due to the material structural destruction. As a result most of the incident energy decays nonradiatively, yielding a strong photothermal radiometric signal. Conversely, in the intact part of the enamel the luminescence is significantly enhanced, while the photothermal contribution is decreased. The two images together represent the expected balance of excited-state energy release between a radiative (luminescence) and a nonradiative (thermal-decay) dynamic process. The PTR image is the result of thermal-wave generation in the tooth and thus consists of two channels; amplitude and phase, Figures 2(b)–2(d). In turbid media, these channels carry thermal transport information within approximately one thermal centroid below the surface. The thermal diffusion centroid is determined as the ''center of mass'' among thermal diffusion length, $\mu = \lambda_{th}/2\pi$, optical absorption depth and optical scattering mean free path in the bulk of the material. Photothermal amplitude is generally more sensitive to surface property variations, such as the reflectance, whereas phase is largely insensitive to the optical properties of the surface and probes a larger depth range[14] into the material. In Figure 3(b), the PTR amplitude exhibits two ''hot spots'' in the defective enamel which approximately correspond to the two spots seen on the backilluminated (transmission) photograph region in Figure 2. These two spots are also seen in phase, Figure 3(c), confirming that the extent of these regions of the crack is deeper into the enamel. From optical observation of the tooth after the scan, it is estimated that the penetration of the crack spots is 300 μm. The luminescence image, Figure 3(a), however, shows the crack damage to be uniform throughout the extent of the crack. This is probably due to the influence of enhanced optical scattering at the crack leading to photon diffusion and ''blurring'' of the luminescence emission from dental enamel and points to the major difference between the two imaging principles: PTR images depth profiles of subsurface heat sources; luminescence does not, but is affected by image ''blurring'' due to photon scattering at the crack. It turns out it is also affected by photon emission delay processes which are characteristic of the material (enamel). Figure 3 further points to the other major difference between the two techniques: the superior dynamic range of the PTR amplitude. For this reason, the image in Figure 3(b) is sliced to allow the visualization of other features, the PTR intensity of, which is much lower than the peaks of the defect regions. The sliced image is seen in Figure 3(d), whose features are now comparable to the PTR phase, Figure 3(c). On the contrary, the luminescence amplitude is essentially continuous along the crack and shows neither the detailed morphology of the cracked region, nor any similarly great signal variations from the surrounding regions.

The dynamic character of modulated imaging (PTR and luminescence) is manifested by scanning imaging at different frequencies. Furthermore, the depth profilometric character of PTR can be assessed in terms of defective enamel information obtained from different depths. These aspects are illustrated by examining a second flat tooth sample with 10–20 μm wide multicrack region. A photograph of the 2 mm thick enamel slice and 3 mm×6 mm in size, taken with the same methodology as Figure 2, is shown in Figure 4. A 0.1 mm×0.2 mm defective region, as shown in Figure 4, of the enamel sample was examined at three frequencies, $f = 30$, 80, and 500 Hz. Visual examination of the cracked region revealed that the surface damage was much less severe than the crack of Figure 2 and that the penetration depth of the deepest rightmost crack was approximately 350 μm. The simultaneous PTR and luminescence images are shown respectively in Figures 5, 6, and 7. In Figure 5(a), the luminescence amplitude signal is dominated by the quality of the enamel. The black regions are intact enamel; the light gray regions signify damaged enamel. The PTR amplitude and phase are seen in Figures 5(b) and 5(c), respectively. At $f = 30$ Hz, the information obtained photothermally is from deep (mm range) into the enamel. Here, again, a comparison with the broader features of Figure 5(a) shows the expected general anticorrelation of signal amplitudes *and* the higher localization of the PTR feature morphologies, consistent with excitation and/or luminescence photon scattering (image blurring) at the defective sites of the enamel. The PTR phase image shows exact correlation with the amplitude image and similarly localized features. The additional details on the right half of the phase image are due to the lower dynamic range of the phase channel. The most striking features of the PTR images are three major defect-cluster regions seen in both amplitude and phase. Furthermore, the amplitude image shows the differences in damage levels, the rightmost crack being the most damaged one, followed by the leftmost crack. The backilluminated photograph in Figure 4, since it is a transmission image, can be compared to the information given for $f = 30$ Hz. In the photograph, the rightmost crack is shown along with the leftmost crack but the middle defect, since it is not as sharp, is not clearly resolved. The broadly anticorrelated luminescence image does not show clear evidence of the crack morphologies. At the higher modulation frequency, $f = 80$ Hz (Figure 6), the same defect region is examined and PTR information about crack regions closer to the surface is obtained. At this subsurface level, the three cracks appear larger and additional defect features have emerged in both PTR amplitude and phase. Comparing the phase, Figure 6(c) with its lower-frequency counterpart, Figure 5(c), it becomes apparent that the damage on the right half side of the image is associated with deeper bulk features, whereas the left side cracks are very close to the

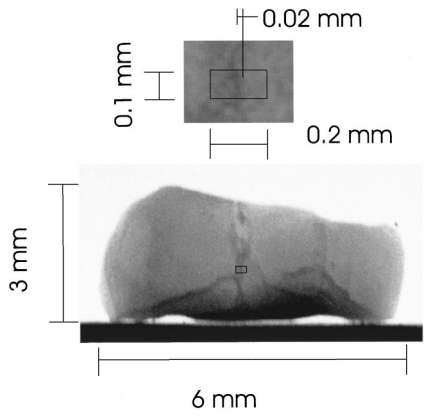

Fig. 4 Backilluminated photograph of a flat enamel slice with a 10–20 μm wide multi-crack region.

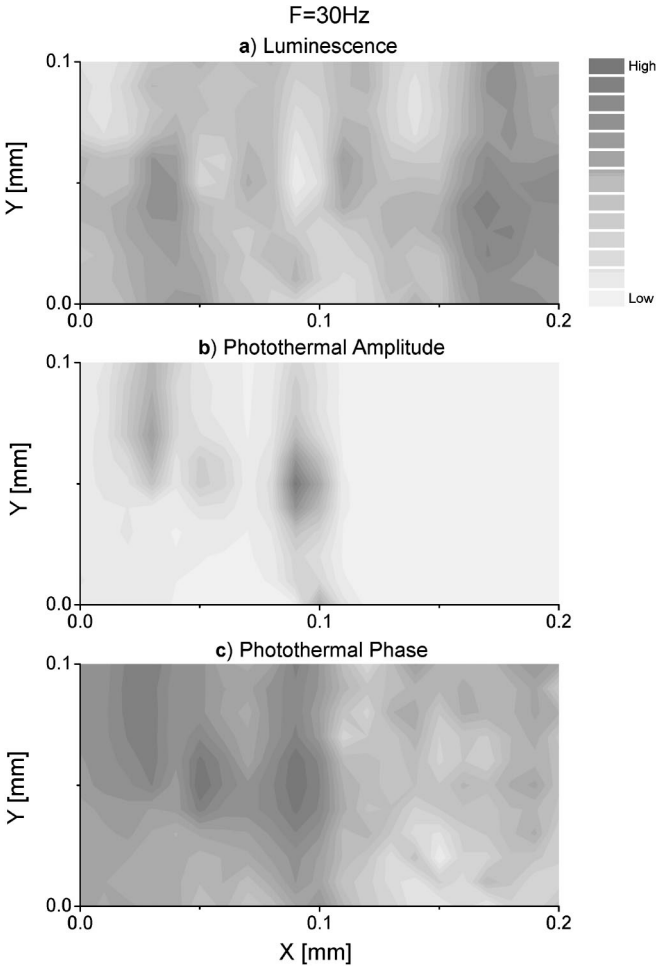

Fig. 5 Simultaneous luminescence and FD-PTR images at $f = 30$ Hz. (a) Luminescence amplitude, (b) PTR amplitude, and (c) PTR phase.

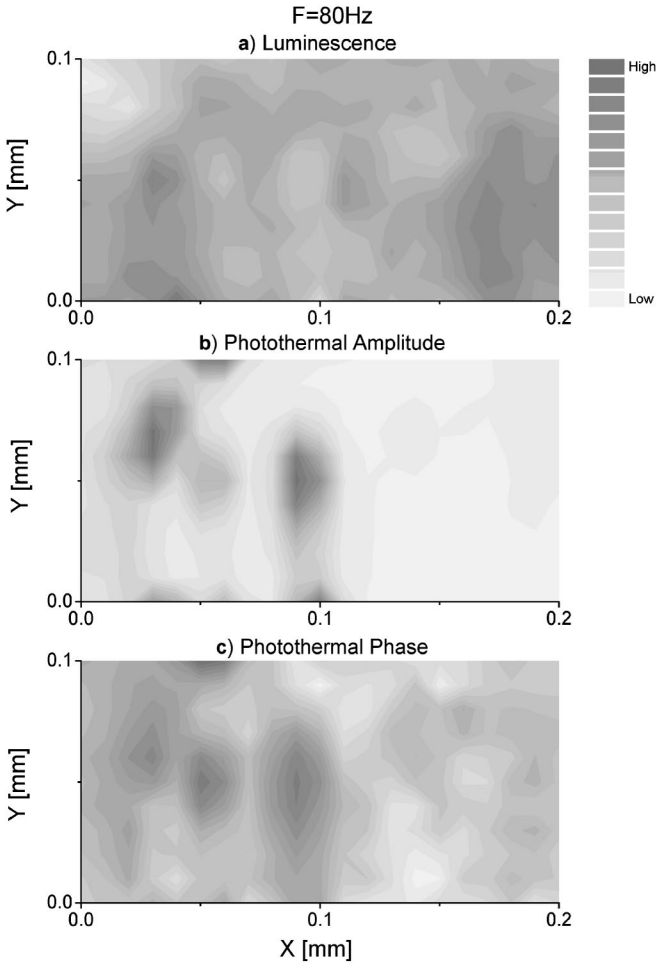

Fig. 6 Simultaneous luminescence and FD-PTR images at $f = 80$ Hz. (a) Luminescence amplitude, (b) PTR amplitude, and (c) PTR phase.

surface. The luminescence image at 80 Hz is only minimally anticorrelated with the PTR images, and this is likely due to scattering delocalization. At $f = 500$ Hz (Figure 7), the PTR images show the best delineation of the very-near-surface morphologies of the three cracks. This amounts to enhanced image resolution compared to Figures 5 and 6, and is expected photothermally, as the wavelength of the thermal wave that interacts with the crack decreases and the thermal emission becomes more localized. It should be noticed from the PTR amplitude image that the very-near-surface extent of the middle crack is more substantial than when deeper regions are probed. The sequence of Figures 5–7(b) indicates that this crack most likely originates at the surface proper. It is interesting to note that all anticorrelation regarding the three cracks with the luminescence amplitude imaging, Figure 7(a), is lost at 500 Hz. Nevertheless, broad anticorrelation exists on the right side of the images between Figures 7(a) and 7(c). In conclusion, the sequence of Figures 5–7 shows that modulated luminescence imaging is most useful at low frequencies and it yields integrated bulk information. A major advantage of dental PTR imaging is the localization of features, largely due to the relative insensitivity of this technique to photon scattering.

3.2 Frequency Scans

From the luminescent and photothermal images of Figures 5–7, it is seen that both dental enamel luminescence and PTR are capable of dynamic imaging, i.e., feature structures depend strongly on modulation frequency. To study these effects, frequency scans in the range of 10 Hz–10 kHz were performed at (visually) intact and cracked regions of the dental enamel and also of the hydroxyapatite sample as a homogeneous reference. Figure 8 shows the simultaneous photothermal and luminescence frequency scans. In Figure 8(a), the PTR amplitude is shown for various spots on the tooth. The signals from good enamel, curve Nos. 1 and 2 are about two orders of magnitude smaller than curve Nos. 3 and 4 from damaged enamel (note the logarithmic scale). This very wide dynamic range of the PTR signal amplitude is consistent with the imaging part of the experiments, specifically Figure 3(b) where the peaks of the damage features had to be sliced off in order to see other lower-level features in the image. It is interesting to note that the signal amplitude from hydroxyapatite is at the same level as the cracked enamel surface. The luminescence amplitudes, Figure 8(c), exhibit the expected anticorrelation with the PTR counterparts, albeit with much lower dynamic range (note the linear scale). The full luminescence

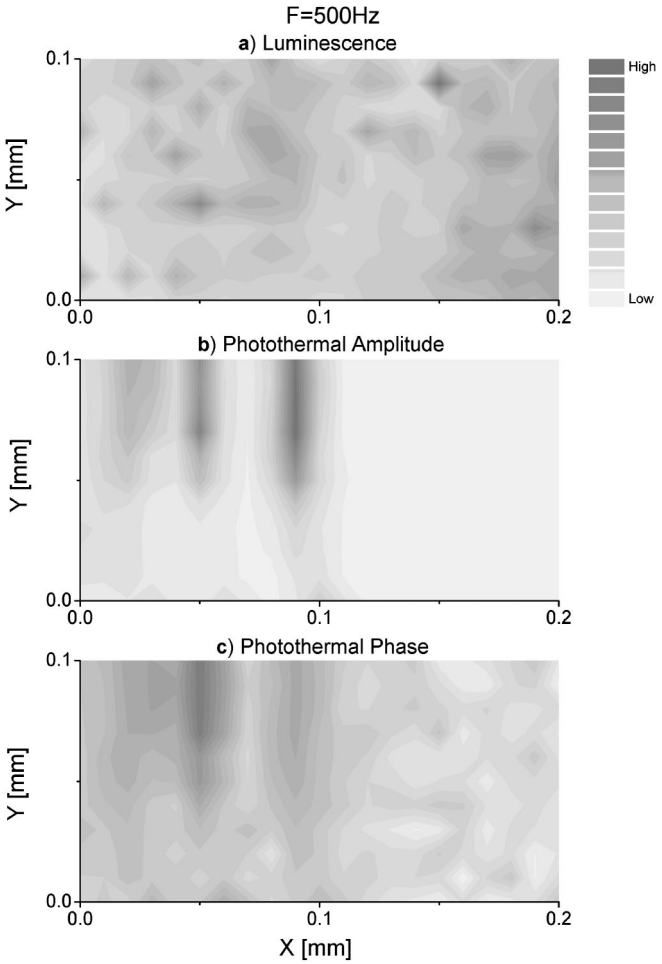

Fig. 7 Simultaneous luminescence and FD-PTR images at $f = 500$ Hz. (a) Luminescence amplitude, (b) PTR amplitude, and (c) PTR phase.

amplitude range between good and cracked enamel is less than a factor of 2. It is interesting that the hydroxyapatite luminescence amplitude is much less than any enamel region, although the curvature of the frequency scan is similar to the other curves. The luminescence phases, Figure 8(d), show no apparent difference between good and cracked enamel. The hydroxyapatite phase is similar to that of the enamel at low frequencies, except for a slight shift in the position of the minimum and the turnaround at high frequencies, which is not observable on the phase data from the particular enamel thin slab of Figure 8. It is important to mention that luminescence phase frequency responses much closer to that of hydroxyapatite, Figure 8(d), are observed with thick intact enamel slices, Figures 10(b) and 10(d).

3.3 Dynamic Luminescence Model

The dental luminescence signal can be explained in terms of the Fourier transform of a time-domain rate model that may involve one multilevel or two independent chromophores. In the case of a single absorber, we assume two luminescent population levels, E_1 and E_2, one of which (E_1) is optically excited directly by the pump laser beam at a rate $W_{P2}(t)$. A fraction N_2 of the population of E_2 decays radiatively to level E_1 generating luminescence photons of energy $h\nu_{21}$. The remaining fraction of E_2 population decays nonradiatively producing heat locally in the neighborhood of the laser beam. The population N_1 of the fluorophore level E_1 is also assumed to decay by emission of luminescence photons of energy $h\nu_{10}$ and through nonradiative channels. Therefore, for practical purposes, both levels contribute to radiative emission in arbitrary proportions in the time domain, with the consequences that these fractions of the populations of E_1 (N_1) and E_2 (N_2) levels can be considered arbitrary and independent of each other. This is further consistent with our experimental

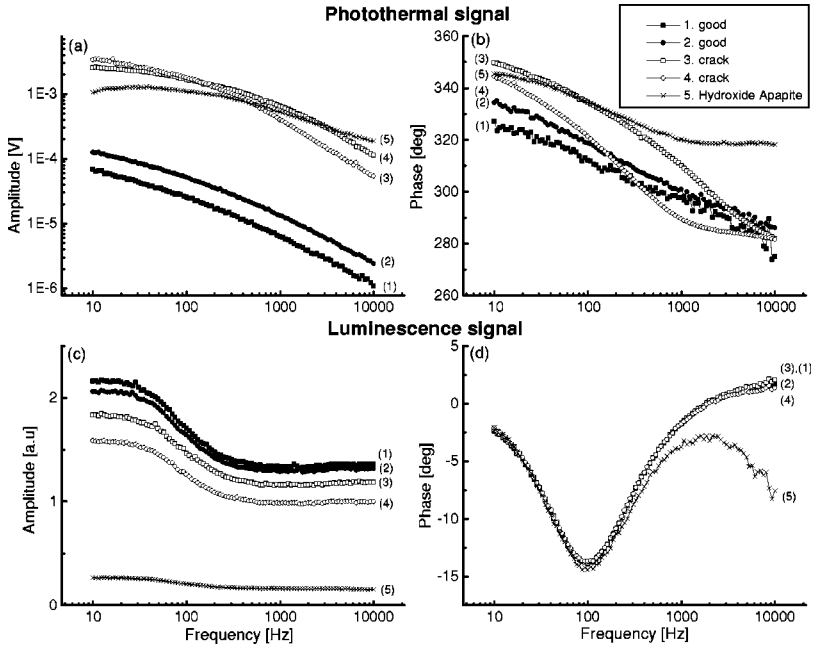

Fig. 8 Simultaneous luminescence and FD-PTR frequency responses from visually intact dental enamel, defective (cracked) dental enamel, and hydroxyapatite. (a) Luminescence amplitude scan, (b) luminescence phase scan, (c) PTR amplitude scan, and (d) PTR phase scan.

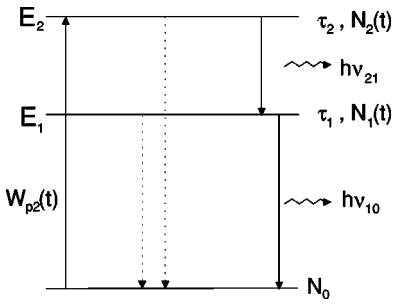

Fig. 9 Two-level fluorophore luminescence emission rate dynamic model. Solid line and dashed arrows correspond to radiative and nonradiative decay, respectively.

results from hydroxyapatite and enamel, according to which models based on full transition of the upper fluorophore state E_2 into the lower state E_1 cannot explain the dynamic luminescence frequency-modulation curves. The rate equations for the two independent photon emission densities N_1 and N_2 are

$$\frac{dN_2(t)}{dt} = W_{p2}(t)N_0(t) - \frac{N_2(t)}{\tau_2} \tag{1a}$$

and

$$\frac{dN_1(t)}{dt} = -\frac{N_1(t)}{\tau_1}, \tag{1b}$$

where $W_{p2}(t)$ is approximated by an impulse $\delta(t)$ on the time scale of our experiments. In Figure 9, h is Planck's constant, 6.63×10^{-34} J s, and ν_{ij} is the frequency (Hz) of a photon emitted following a transition between levels (i) and (j). The photon energy is $E_{ij}=h\nu_{ij}$. From the solution of Eqs. (1a) and (1b), the total temporal photon emission density, $N_T(t)$ is

$$\begin{aligned} N_T(t) &= N_1(t) + N_2(t) \\ &= N_{T1}\exp(-t/\tau_1) + N_{T2}\exp(-t/\tau_2), \end{aligned} \tag{2}$$

where N_{T1} and N_{T2} are the occupation densities of level E_1 and E_2, respectively, at time $t=0$, i.e., at the onset of the luminescence emitting decay. It is assumed that (as yet unspecified) molecular or electronic radiative processes are responsible for the emission of luminescence. Accordingly, the two levels in Figure 9 can take on the meaning of molecular or electronic excited states. τ_1 and τ_2 are the two characteristic luminescence decay times of the system. The foregoing model with essentially independent populations N_1 and N_2 is also valid for the case of two independent fluorophores, each of which possesses at least two energy levels as shown in Figure 9 and can absorb the same-energy photon $h\nu_{20}$. Assuming luminescence decay lifetimes τ_1 and τ_2 for each fluorophore and independent nonradiative decay rates, the resulting luminescence population transient is given, again, by Eq. (2). The modulation-frequency dependence of the total photon emission density, $\rho(\omega)$, is given by Fourier transforming Eq. (2),

$$\rho(\omega) = N_{T1}\frac{1}{i\omega+\tau_1^{-1}} + N_{T2}\frac{1}{i\omega+\tau_2^{-1}}. \tag{3}$$

In Figure 10, theoretical fits of the foregoing two-level model to the amplitude and phase of the luminescence frequency scans are shown for hydroxyapatite, Figures 10(a) and 10(b); a sound premolar tooth sample without dentin removal

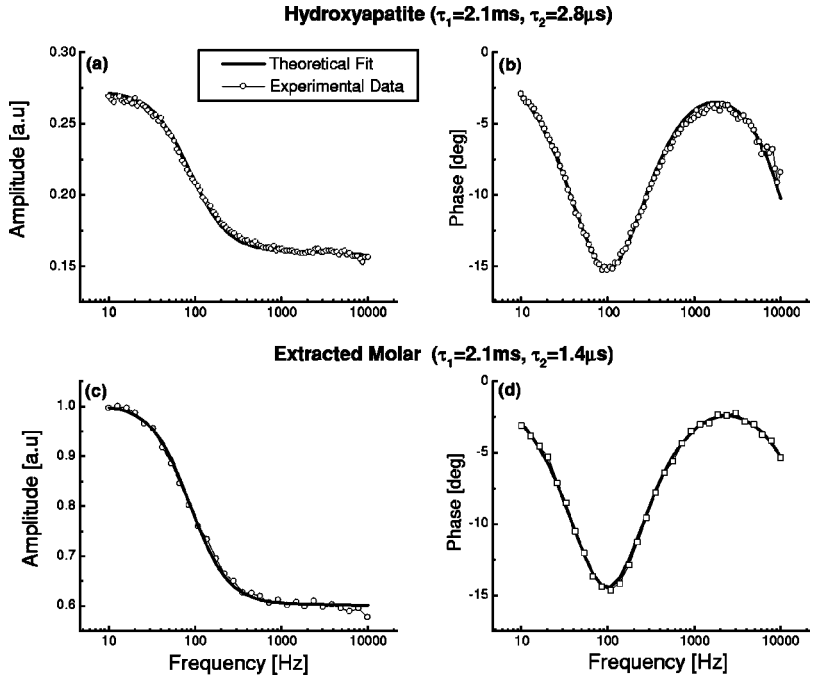

Fig. 10 Theoretical fits using the theoretical model of Fig. 9 to luminescence frequency responses. (a) Hydroxyapatite signal amplitude, (b) hydroxyapatite signal phase, (c) signal amplitude from visually intact dental enamel of extracted molar, (d) signal phase corresponding to (c).

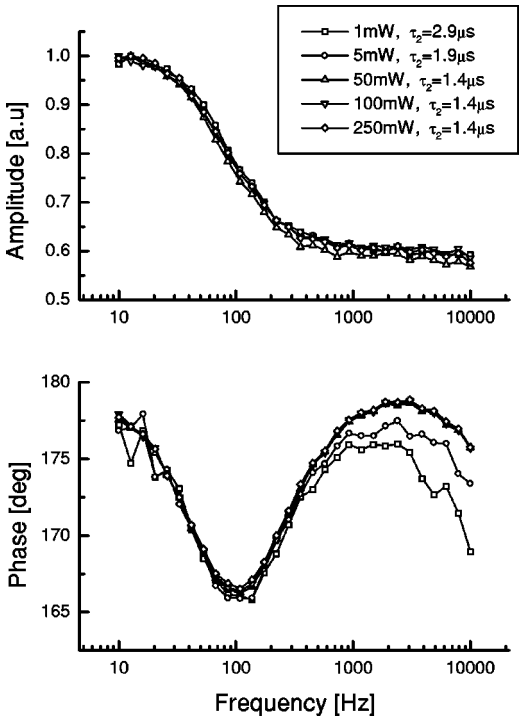

Fig. 11 Luminescence frequency responses from visually intact dental enamel of extracted premolar. (a) Luminescence amplitude, (b) luminescence phase.

was also fitted, Figures 10(c) and 10(d). It is found that one luminescence lifetime (τ_1) is associated with the first (lowest) minimum of the phase and that the other luminescence lifetime (τ_2) is associated with first (highest) maximum of the phase. There is no distinction between hydroxyapatite and good enamel regarding the value of this lifetime: $\tau_1 = 2.1$ ms. The second lifetime is more sensitive to the particular specimen and is associated with a higher-frequency maximum in phase. It is observed that the second maximum moves to higher frequencies as the second lifetime decreases. The hydroxyapatite data can be fitted into a lifetime of $\tau_2 = 2.8$ μs, whereas the enamel has a smaller lifetime of $\tau_2 = 1.4$ μs. There have been no previous reports on the long lifetimes observed in our experiments. Dental relaxation lifetimes on the ns scale from carious dental enamel have been reported by Alfano et al.[15] using ultrafast laser detection of luminescence. For the experimental results from the thin enamel sample shown in Figure 8, the theory departs from the experimental data at the high frequency end, and the second lifetime of the order of μs cannot be fitted. It is clear that more work is needed in interpreting the origin(s) of the two relaxation times of Figures 8 and 10. With the exception of the thin enamel sample of Figure 8, in general, the model has been able to fit a large set of samples as it did with the hydroxyapatite and the sound enamel samples of Figure 10.

The effect of the laser fluence on the sample luminescence frequency response was also studied. Figure 11 shows amplitude and phase curves for 1, 5, 50, 100, and 250 mW incident power. There appears to be some degree of photobleaching at the high-frequency end of the luminescence phase scan for laser powers as low as 1 mW, which saturates for powers on the order of 50 mW. The net effect of the laser power increase shows up as a decrease of the shorter lifetime, τ_2, by a factor of 2. There is no shift in the minimum of the luminescence phase but there is some effect at the high-frequency end. Above the 50 mW range, there is no effective change, and the shorter lifetime associated with these experiments is $\tau_2 = 1.4$ μs. For 5 and 1 mW, the shorter relaxation time is 1.9 and 2.9 μs, respectively. From these measurements, we conclude that the longer lifetime τ_1 remains insensitive to the laser fluence, with some bleaching and saturation of the faster fluorophore exhibited at high laser fluences.

In view of this dynamic (delay-time) structure of the luminescence behavior, it can be said that the high-frequency luminescence amplitude images in Figures 5–7 contain some lifetime contrast information. The low-frequency images have no contrast related to the long lifetime τ_1, because its value is the same for all intact and damaged regions of the enamel alike. The frequency dependence of the PTR curves is currently under theoretical examination.

4 Conclusions

Frequency-domain infrared photothermal radiometry (FD-PTR) was introduced as a nondestructive, nonintrusive method for evaluating sound and defective tooth enamel, and was shown to be a complimentary imaging technique to luminescence. Several advantages of FD-PTR imaging were found including much superior dynamic range of the amplitude signal with regard to the defect state of dental enamel, superior feature localization and resolution, and depth profilometric capabilities. A theoretical model to explain the frequency dependence of luminescence emission was advanced and two characteristic lifetimes were measured. The longer of the two lifetimes was common in intact and cracked enamel and in hydroxyapatite and, therefore, it can be associated with the chemical and excited-state molecular or electronic structure of these mineral compounds.

Acknowledgments

The support of Materials and Manufacturing Ontario (MMO) is gratefully acknowledged. The authors wish to thank Dr. Robert M. Pillar for providing them with a hydroxyapatite sample.

References

1. V. D. Rijke and J. J. ten Bosch, ''Optical quantification of caries like lesions *in vitro* by use of fluorescent dye,'' *J. Dent. Res.* **69**, 1184–1187 (1990).
2. J. Baron, K. Zakariasen, and B. Patton, ''Detecting CO_2 laser effects by 3D image scanned laser fluorescence,'' *J. Dent. Res.* **72**, special issue #1060, 236 (1993).
3. C. D. Gonzalez, K. Zakariasen, D. N. Dederich, and R. J. Pruhs, ''Potential preventive and therapeutic hard tissue applications of CO_2 and Nd:YAG and Argon lasers in dentistry: A review,'' *J. Dent. Child* **May-June**, 196–207 (1996).
4. M. Munidasa, T. C., A. Mandelis, S. K. Brown, and L. Mannik, ''Non-destructive depth profiling of laser processed Zr-2.5Nb alloy by infrared photothermal radiometry,'' *Mater. Sci. Eng., A* **159**, 111–118 (1992).
5. G. Walther, ''Photothermal nondestructive evaluation of materials with thermal waves,'' in *Progress in Photothermal and Photoacoustic Science and Technology*, A. Mandelis, Ed., Vol. 1, pp. 205–298, Elsevier, New York (1992).
6. A. Mandelis, M. Munidasa, and A. Othonos, ''Single-ended infrared

photothermal radiometric measurements of quantum efficiency and metastable lifetime in solid-state laser materials: the case of ruby (Cr^{3+}:Al_2O_3),'' *IEEE J. Quantum Electron.* **29**, 1498–1504 (1993).
7. A. J. Welch and M. J. C. van Gemert, Ed., in *Optical-Thermal Response of Laser-Irradiated Tissue*, Plenum, New York (1995).
8. S. A. Prahl, A. I. Vitkin, U. Bruggemann, B. C. Wilson, and R. R. Anderson, ''Determination of optical properties of turbid media using pulsed photothermal radiometry,'' *Phys. Med. Biol.* **37**, 1203–1217 (1992).
9. D. Fried, W. Seka, R. E. Glena, and J. D. B. Featherstone, ''Thermal response of hard dental tissues to 9- through 11-μm CO_2-laser irradiation,'' *Opt. Eng. (Bellingham)* **35**, 1976–1984 (1996).
10. D. Fried, S. R. Visuri, J. D. B. Featherstone, J. T. Walsh, W. Seka, R. E. Glena, S. M. McCormack, and H. A. Wigdor, ''Infrared radiometry of dental enamel during Er:YAG and Er:YSGG laser irradiation,'' *J. Biomed. Opt.* **1**, 455–465 (1996).
11. A. Mandelis, ''Signal-to-noise ratios in lock-in amplifier synchronous detection: A generalized communications system approach with application to frequency-, time-, and hybrid (rate-window) photothermal measurements,'' *Rev. Sci. Instrum.* **65**, 3309–3323 (1994).
12. L. Nicolaides, M. Munidasa, and A. Mandelis, ''Thermal-wave diffraction tomographic microscopy,'' IIII International Workshop-Advances in Signal Processing for NDE of Materials, Vol. 3, X. P. V. Maldague, Ed., in *Topics on Nondestructive Evaluation Series,* Am. Soc. Nondest. Test. Inc., Columbus, OH (1998).
13. F. Sundstrom, K. Fredricksson, S. Montan, U. Hafstorm-Bjorkman, and J. Strom, ''Laser-induced fluorescence from sound and carious tooth substance: Spectroscopic studies,'' *Swed. Dent. J.* **9**, 71–80 (1985).
14. G. Busse, ''Optoacoustic and photothermal inspection techniques,'' *Appl. Opt.* **21**, 107 (1982).
15. R. R. Alfano and S. S. Yao, ''Human teeth with and without dental caries studies by visible luminescent spectroscopy,'' *J. Dent. Res.* **60**, 120–122 (1981).